IEEE Access
Multidisciplinary | Rapid Review | Open Access Journal

Received October 6, 2018, accepted October 21, 2018, date of publication October 24, 2018, date of current version November 30, 2018.

Digital Object Identifier 10.1109/ACCESS.2018.2877844

Interdigitated Horizontal Electrodes for Organic Solar Cells

YOUNG-JUN YOU, DO YOUNG KIM, SANG-CHUL SHIN, AND JAE WON SHIM

[1]Division of Electronics and Electrical Engineering, Research Center for Photoenergy Harvesting & Conversion Technology, Dongguk University, Seoul 04620, South Korea

Corresponding author: Jae Won Shim (jwshim@dongguk.edu)

This work was supported in part by the Basic Science Research Program through the National Research Foundation (NRF), South Korea, the Ministry of Science, ICT & Future Planning (NRF), under Grant 2015R1C1A1A01051841, in part by the Technology Development Program to Solve Climate Changes of the NRF through the Ministry of Science, ICT & Future Planning (NRF) under Grant 2016M1A2A2940912, and in part by the Korea Institute of Energy Technology Evaluation and Planning (KETEP) under Grant 20174030201520.

ABSTRACT We first introduce a new electrode structure for organic solar cells (OSCs), the so-called interdigitated horizontal electrode (IHE), in which an electron-collecting electrode and a hole-collecting electrode are horizontally separated. In the IHE, the directions of the incident light and the charge collection are perpendicular to each other. Therefore, the thickness of the photoactive layer is no longer limited by the poor electrical mobility of the carriers in the organic-based photoactive layer. An analysis of the electrical, optical, and electrochemical properties of the IHE is presented. For poly(3-hexylthiophene) (P3HT):[6,6]-phenyl C_{60} butyric acid methyl ester ($PC_{60}BM$)-based IHE OSCs, a proof-of-principle demonstration is performed of their feasibility as electrodes. Such OSCs yielded a power-conversion efficiency of $1.2 \pm 0.1\%$, with a short-circuit current density (J_{SC}) of 13.6 ± 0.2 mA/cm^2, which is larger than the J_{SC} of 8.5 ± 0.2 mA/cm^2 of the reference OSCs with their conventional stacked structure.

INDEX TERMS Interdigitated horizontal electrodes (IHE), organic solar cells (OSCs), high short-circuit current density (J_{SC}), finite-difference time-domain (FDTD) simulation.

I. INTRODUCTION

Organic solar cells (OSCs) have attracted considerable attention because of their excellent features such as tunable optical and electrical properties of the organic material and viability for adoption of low-cost and simple fabrication method as a promising future renewable energy harvester [1]–[10]. Recently, considerable effort has been made to synthesize noble photoactive materials and develop device geometries. As a result, a power-conversion efficiency (PCE) of up to 14% has been reported [11].

Despite such recent advance, several inherent issues due to the device geometry of the OSCs still limit their photovoltaic performance. OSCs are generally composed of a photoactive layer sandwiched between two charge-collecting electrodes (CCEs), one of which should have high optical transmittance to allow the large number of photons to pass through. Up to now, a variety of conducting materials have been utilized as transparent electrodes, such as transparent conductive oxides, conducting polymers, metal nano wires (or particles), etc [4], [6], [12]–[14]. However, due to the absorption from the transparent electrodes, an optical loss of more than 10% inevitably occurs, which has a negative impact on short-circuit current density (J_{SC}) since the J_{SC} is known to be directly proportional to the light absorption. In addition, due to the relatively low carrier mobility of the organic semiconductor, the allowable photoactive layer thickness of the OSCs is limited by the transit-time of the carriers within the photoactive layer [15].

To overcome these issues, interdigitated back contact (IBC) structures have often been used in silicon-based solar cells. In IBC structures, both an electron-collecting electrode (ECE) and a hole-collecting electrode (HCE) are buried inside the silicon photoactive layer, while in a conventional structure, the ECE and HCE are stacked on either side of the photoactive layer [16], [17]. The IBC structure allows maximum light absorption because the reflective metal electrode is not fabricated on the light-receiving surface. It also allows optimum charge-collection efficiency since it enables the minimized travel distance of the charge carriers, electrons, and holes.

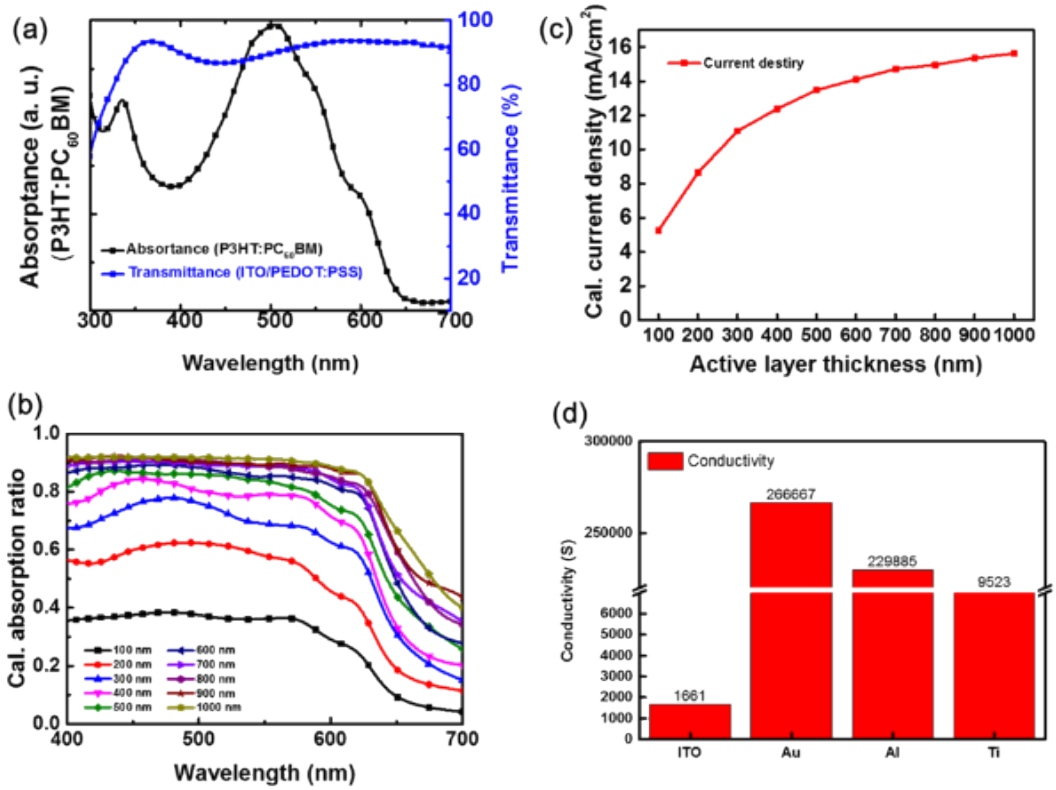

FIGURE 1. **(a) Comparison between the transmittance of the ITO/PEDOT:PSS substrate and the absorptance of the P3HT:PC_{60}BM. (b) Calculated absorption spectra of P3HT:PC_{60}BM with various thicknesses. (c) Calculation of the highest possible current density of the P3HT:PC_{60}BM OSC (100% IQE) with various thicknesses. (d) Conductivity values of charge-collecting electrodes (ITO, Au, Al and Ti).**

Recently, Yoshikawa *et al.*, demonstrated the heterojunction (HJ)-IBC silicon solar cell with a PCE exceeding 26.3 % [18], [19]. In addition, Hou *et al.* [20] reported the use of the interdigitated electrodes for perovskite solar cells, providing unprecedented J_{SC} values higher than 16 mA/cm^2 under solar illumination.

The IBC structure can be a promising electrode design for OSCs for the following reasons. (i) In the IBC structure, the use of CCEs at the light receiving side is avoided, and thus the optical loss induced from the absorption of the CCEs is minimized. In addition, in the IBC structure, the thickness of the photoactive layer is no longer limited by the transit-time of the carriers because the light incident direction and the charge carrier diffusion direction are perpendicularly separated [21]. However, since the mobility of the organic semiconductor is less than that of the silicon, the single organic semiconductor located between the ECE and HCE serves as the photoactive layer. Therefore, in order to employ the IBC structure in OSCs, its spacing size needs to be further reduced and the height of the electrodes needs to be precisely controlled [15].

Here, we first demonstrate OSCs with horizontally positioned ECE and HCE, the interdigitated horizontal electrodes (IHEs). The IHE with about 1.5 μm-long horizontal spacing between the ECE and HCE was fabricated on silicon dioxide (SiO_2)-deposited silicon substrates using precise photolithography. A large work function (WF) contrast between the two electrodes was realized by adopting Au as the large WF metal ($\sim$ 5.1 eV) and Al ($\sim$4.2 eV) as the small WF metal. The morphological and optical properties of the IHE-based OSCs were evaluated by atomic force microscopy (AFM) and ultraviolet–visible (UV–vis) spectrometry. In addition, the finite-difference time-domain (FDTD) method was utilized to evaluate the effects attributed to the electrode structures on the device performance and to estimate the photoactive layer thickness required to produce the optimum J_{SC}. Optimized poly (3-hexylthiophene) (P3HT):[6, 6]-phenyl C_{60} butyric acid methyl ester (PC_{60}BM)-based OSCs with the 400 nm-thick IHE were shown to yield a PCE of 1.2 $\pm$ 0.1%, with a significantly large J_{SC} value of 13.6 $\pm$ 0.2 mA/cm^2 under an air mass (AM) of 100 mW/cm^2 and solar illumination of 1.5 global (G).

II. RESULTS AND DISCUSSION

Before describing the device performance, the optical and electrical properties of the IHEs and the thin film characterization of the P3HT:PC_{60}BM photoactive layer are discussed. Figure 1(a) shows a comparison between the transmission spectra of the ITO / PEDOT:PSS HCE and the absorptance of

the P3HT:PC_{60}BM photoactive layer. The ITO/PEDOT:PSS HCE exhibited an optical loss of more than 10 % in the spectral region of interest corresponding to the absorption range of the P3HT:PC_{60}BM photoactive layer (410 nm–630 nm), consistent with the previous reports in the literature [22]–[24]. Meanwhile, in the IHE case, the absence of the transparent electrodes at the light receiving side means that optical loss is avoided, leading to maximized light absorption in the photoactive layer.

To evaluate the thickness effect of the photoactive layers on the J_{SC}, a finite-difference time-domain (FDTD) simulation was carried out. As shown in Figure 1(b), the simulated light absorption increased in proportion to the photoactive layer thickness, and was saturated with a photoactive layer of approximately 500-nm-thick. The saturation of the light absorption seems to be related to the penetration depth of the photoactive layer, suggesting maximum metal ECE and HCE thickness. Based on the results of the absorption simulation, the maximum J_{SC} values achievable with each thickness were calculated (Figure 1(c)). The J_{SC} value of approximately 5 mA/cm^2 was expected from the 100-nm-thick photoactive layer. The calculated J_{SC} value was shown to increase with the thickness and the J_{SC} saturation value was reached at approximately 14 mA/cm^2 with a 500-nm-thick photoactive layer, which is in good agreement with the absorption simulation. Moreover, while in the conventional structure, the transparent electrodes such as ITO are located on one side of the device, in the IHE structure, reflective metals are used with high conductivity (shown in Figure 1(d)) for both the ECE (Al and Ti) and HCE (Au) sides, and thus a minimized resistive power loss is obtained.

The thickness-dependent morphological change of the P3HT:PC_{60}BM photoactive layer was investigated using atomic force microscopy (AFM). Photoactive layers with four different thicknesses (200 nm, 300 nm, 440 nm, and 9.18 μm) were prepared on glass/ITO substrates. The thicknesses were controlled by the spin-coating rate (0 rpm for 1 min: 9.18 μm; 300 rpm for 1 min: 440 nm; 500 rpm for 1 min: 300 nm; and 700 rpm for 1 min: 200 nm). Figures 2(a)-(d) show the AFM images obtained from each photoactive layer. From these images, the root-mean-squared (RMS) surface roughness values were derived, having an area of 1 μm^2. Any significant variation in the RMS surface roughness values (200 nm: 0.78 nm; 300 nm: 0.8 nm; 440 nm: 1.03 nm; 9.18 μm: 1.38 nm) was not detected. These results imply that, rather than the morphologies of the photoactive layer, other factors such as the penetration depth and the carrier transit time might be responsible for the current generation [22].

Figure 3(a) shows the device structure of the P3HT:PC_{60}BM-based IHE OSCs and the chemical structures of the P3HT and PC_{60}BM. The IHE was fabricated on a 150-nm-thick SiO_2-deposited Si substrate. A 300-nm-thick SiO_2 layer was employed to facilitate the photolithography process and to insulate the two horizontally positioned electrodes. 200-nm-thick, 300-nm and 400-nm-thick Al layers served as the ECE, and Au layers having the same thicknesses

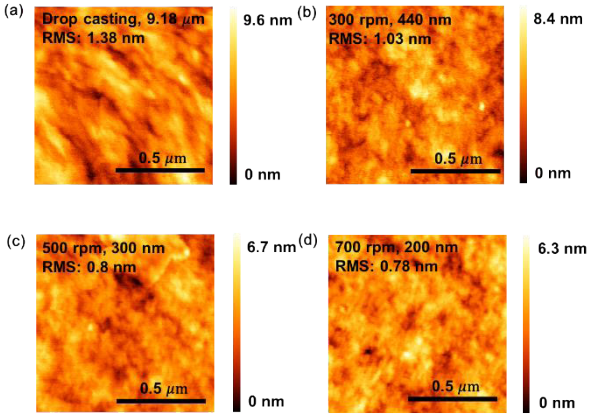

FIGURE 2. AFM images of the P3HT:PC_{60}BM with layer thicknesses of (a) 9.18 μm, (b) 440 nm, (c) 300 nm, and (d) 200 nm.

worked as the HCE. The 1.5 μm-long distance between the HCE and ECE were accurately estimated from the focused ion beam (FIB) image shown in Figure 3(b). In addition, to evaluate IHE OSCs performance as a function of the types of electrodes and distance between the HCE and ECE, the Al ECEs were replaced with 300-nm-thick Ti ECEs with varying distances (1.5, 2, and 3 μm). These distance values were carefully estimated using optical microscope images. Defining IHEs having submicron distance IHEs with different metals from the photolithography process was beyond the scope of this current research, it is currently being carried out through other studies. As reference devices, three conventional OSCs with the structures of indium tin oxide (ITO) / PEDOT:PSS / P3HT:PC_{60}BM / Ca / Al (Reference Device A), ITO / PEDOT:PSS / P3HT:PC_{60}BM / Al (Reference Device B), and ITO / P3HT:PC_{60}BM / Al (Reference Device C) were separately fabricated (Figure 3(c)). In the reference devices, the neat ITO or the high-WF (~5.1 eV) PEDOT:PSS-modified ITO substrates served as the HCE at the bottom of the devices, and low-WF Ca / Al (~2.9 eV), Al (~4.2 eV), or Ti (~4.3 eV) at the top of the devices served as the ECE. The thickness of the photoactive layers of the reference devices was about 240 nm. Figure 3(d) illustrates the energy levels of each layer of the IHE OSC and the conventional OSC.

Figures 4(a) and 4(b) compare the current density-voltage (J-V) characteristics measured in the IHE (200 nm, 300 nm and 400 nm) OSCs and the Reference Devices A, B, and C under 1-sun illumination (I_L: 100 mW/cm^2) and in the dark. It is interesting to note that the thickness of the photoactive layers was mainly determined from the spin speed rather than from the electrode thickness. Here, we employed 300 rpm and 500 rpm to provide 400-nm-thick and 300-nm-thick photoactive layers, respectively. The OSCs with the 300-nm-thick IHE yielded a PCE value of 1.0% $\pm$ 0.1% with an open-circuit voltage (V_{OC}) value of 369 $\pm$ 9 mV, a J_{SC} of 13.4 $\pm$ 0.2 mA/cm^2, and a fill factor (FF) of 22.1 $\pm$ 0.4%. The OSCs with the 400-nm-thick IHE showed a comparable performance (with a PCE value of 1.2% $\pm$ 0.1%)

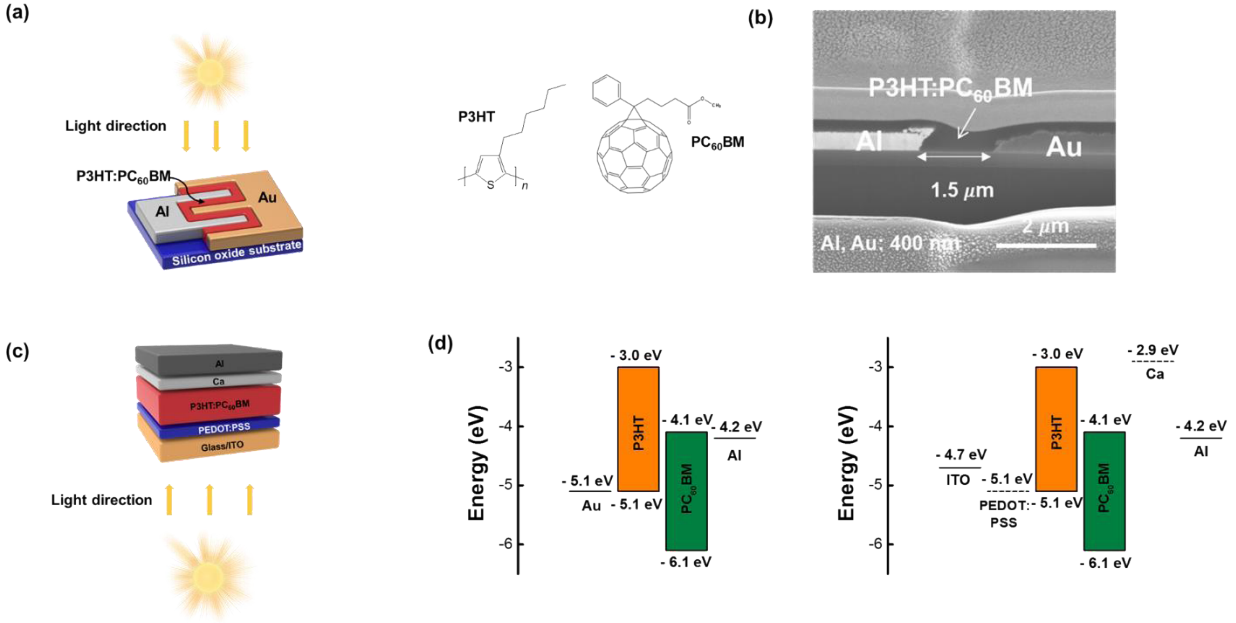

FIGURE 3. (a) Schematic illustration of an IHE structured OSC and the chemical structures of P3HT and $PC_{60}BM$. (b) Cross-sectional FIB image of the IHE structured OSC. (c) Schematic illustration of a conventional stack structured OSC. (d) Energy level diagram of the IHE structured OSC (left) and the conventional stack structured OSC (right).

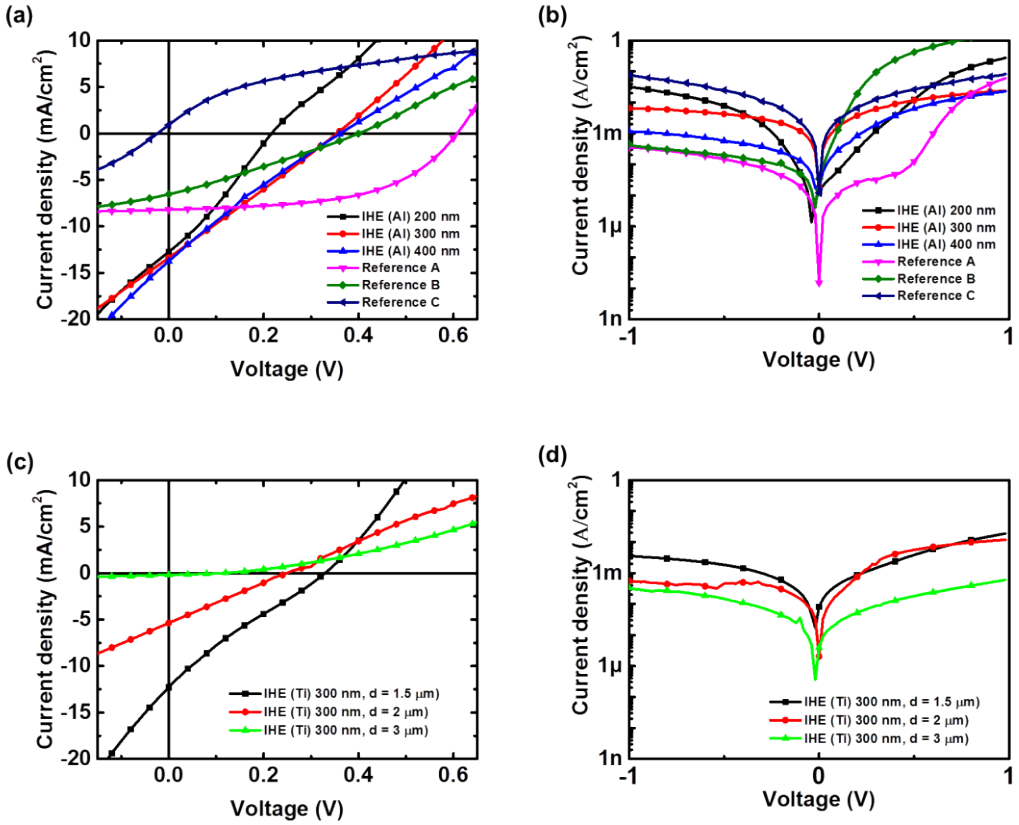

FIGURE 4. Current density-voltage (J-V) characteristics of the IHE structured OSCs (Al and Au) and the conventional stack structured OSCs (a) under 1-sun illumination and (b) in the dark. (c) J-V characteristics of the IHE structured OSCs (Ti and Au) under 1-sun illumination and (d) in the dark.

to that of the 300-nm-thick IHE devices. Reference Device A exhibited excellent performance, with a PCE value of 2.8% ± 0.2%, a V_{OC} value of 606 ± 4 mV, a J_{SC} of 8.5 ± 0.2 mA/cm^2, and a FF of 54.2% ± 1.1%. Reference Device B showed poorer performance, with a PCE value of 0.7% ± 0.1% (V_{OC}: 408 ± 14 mV, J_{SC}: 6.1 ± 0.4 mA/cm^2,

and FF: 26.9% ± 2.8%), which was lower than that of Reference Device A. The degraded performance of the Reference Device B as compared to that of Reference Device A could be attributed to the absence of the Ca electron-collecting interlayer (ECI). Without the ECI, Schottky barrier can be formed due to the energy level misalignment between the WF of Al and the lowest unoccupied molecular orbital (LUMO) of $PC_{60}BM$, leading to a large contact resistance. The high contact resistance limits the electron transfer from $PC_{60}BM$ and the Al ECE, inducing the charge recombination increase resulting in the performance degradation including more than 50 % lowered FF value (26.9 % ± 2.8 %). Finally, Reference Device C did not exhibit photovoltaic performance [25]–[27]. These performance parameters, averaged over the five devices, of all OSCs evaluated are summarized in Table 1.

TABLE 1. Averaged[a] photovoltaic performance parameters of the IHE structured OSCs and the conventional structured OSCs under 1-sun illumination (100 mW/cm^2).

Devices IHE (Au/Al)	V_{OC} (mV)	J_{SC} (mA/cm^2)	FF (%)	PCE (%)
IHE 200 nm	217±0	12.8±0.4	28.4±0.1	0.7±0.3
IHE 300 nm	369 ± 9	13.4 ± 0.2	22.1 ± 0.4	1.0 ± 0.1
IHE 400 nm	356 ± 4	13.6 ± 0.2	25.7 ± 0.2	1.2 ± 0.1
Reference A	606 ± 4	8.5 ± 0.2	54.2 ± 1.1	2.8 ± 0.2
Reference B	408 ± 14	6.1 ± 0.4	26.9 ± 2.8	0.7 ± 0.1

Averaged values were obtained from measurements for five devices.

The IHE devices have J_{SC} values larger than those of Reference Devices A and B partly because of the thicker photoactive layers. It is believed that the thicker photoactive layer induced an increase in light absorption, thus leading to the enhancement of the J_{SC} [15]. While the transit-time of the carriers in the photoactive layers of Reference Devices A and B generally limits the thickness of the photoactive layer by approximately 200 nm, in the IHE cases, the thickness of the photoactive layer can be increased by up to the penetration depth (λ(600 nm): ∼ 233 nm) of the P3HT:$PC_{60}BM$ photoactive layer, leading to a further improved J_{SC}. The increase of the J_{SC} values from 12.8 ± 0.4 mA/cm^2 to 13.6 ± 0.2 mA/cm^2 as the IHE thickened (200 nm → 400 nm), also supports this result. Another viable reason for the J_{SC} increase is the avoidance of the ITO or ITO/PEDOT:PSS transparent electrodes. An absorption of ITO/PEDOT:PSS in the spectral region of interest of approximately 10% may cause a reduction in the number of photons entering in the photoactive layer, resulting in the J_{SC} decrease [28]. Furthermore, the metal-based IHEs appeared to reduce the resistive effects on the performance, leading to the J_{SC} enhancement in the IHE-based devices. The IHE OSCs with Ti ECE (d = 1.5 μm) exhibited a performance comparable to that of the IHE OSCs with the Al ECE (d = 1.5 μm) with a PCE of 0.9 ± 0.2 %.

In addition, it was observed that the J_{SC} values decreased with increase in the distance between the ECE (Ti) and HCE (Au) while the IHE OSCs with Ti ECE (d = 3 μm) hardly operated. The smaller V_{OC} values of the IHE-based OSCs and Reference Device B, compared with that of Reference Device A could have resulted from the larger WF value of Al and Ti than that of Ca [29] Typically, the V_{OC} is limited by the quasi-Fermi level difference between the donor and acceptor materials of the photoactive layer when the WF of the HCE is sufficiently large and the ECE has a low WF value. However, in the cases of the IHE-based OSCs and Reference Device B, the energy-level mismatching between the EA of the $PC_{60}BM$ and the WF of the Al and Ti can induce potential loss, leading a dramatic reduction of the V_{OC} values. As discussed in the previous paragraph, the contact resistance induced from this energy-level mismatching is also responsible for the poor FF values of the IHE devices. As shown by the device results, the main limitation on the performance of the IHE devices is the small V_{OC} and poor FF values (ascribed to the use of the relatively large WF ECE (Al)), rather than the structural properties of the IHEs. This issue can be simply overcome by adopting low WF ECEs. Low WF ECEs can be realized by covering the high WF electrodes with low WF metal oxides including ZnO and TiO_2 or performing a surface modification with amine-containing polymeric surface modifiers such as polyethylenimine ethoxylated (PEIE) [30]–[32]. Further research is currently being conducted to obtain the low WF ECEs for the IHEs. A summary of the performance parameters of the IHE-based OSCs is tabulated in Table 1 and Table 2.

TABLE 2. Averaged[a] photovoltaic performance parameters of the IHE structured OSCs (Au/Ti) with different distances (1.5, 2, and 3 μm) under 1-sun illumination (100 mW/cm^2).

Devices IHE (Au/Ti)	V_{OC} (mV)	J_{SC} (mA/cm^2)	FF (%)	PCE (%)
IHE (300 nm) (d =1.5 μm)	329 ± 10	13.2 ± 4.4	22.0 ± 2.4	0.9 ± 0.2
IHE (300 nm) (d = 2 μm)	218 ± 85	5.0 ± 3.0	19.6 ± 3.0	0.2 ± 0.1
IHE (300 nm) (d = 3 μm)	-	-	-	-

Averaged values were obtained from measurements for five devices.

III. CONCLUSIONS

In this study, we first demonstrated the use of IHEs for the OSCs. The optical and electrical properties of the IHE were investigated and the thickness-dependent achievable J_{SC} values of the OSCs were calculated with the FDTD simulation.

With the IHE, the thickness of the photoactive layer can be maximized because the incident direction of light and the direction of the charge collection are perpendicular to each other, thus maximizing the J_{SC}. In addition, the high conductivity metal-based HCE (Au) and ECE (Al) were believed to contribute to minimizing the resistive loss, leading to the J_{SC} enhancement. Under a simulated illumination of AM 1.5G 100 mW/cm^2, the IHE OSCs with the P3HT:$PC_{60}BM$ photoactive layer showed J_{SC} values of 13.6 ± 0.2 mA/cm^2, which were approximately two times larger than the J_{SC} value (6.1 ± 0.4 mA/cm^2) of the OSC with the stacked conventional structure having similar device components. While providing a sub-micron distance and a large WF contrast between the two metal electrodes remains a challenge, this is currently being investigated in another study. Once resolved, such electrode configuration can be utilized in a variety of thin-film based electronic devices, including organic light emitting transistors and organic thin film transistors.

IV. EXPERIMENTAL SECTIONS

A. ELECTRODES AND P3HT:$PC_{60}BM$ THIN FILM ANALYSIS

A focused ion beam (FIB, QUAMTA 200 3D) was used to analyze the interface and structure of the IHE device. AFM analysis was performed on a photoactive material film deposited on a glass / ITO substrate using a multimode atomic force microscope (TT-AFM, AFM Workshop, Signal Hill, CA, USA). The WF of each material was determined using a Kelvin probe (Besocke Delta Phi, Jülich, Germany) in ambient air. A highly oriented pyrolytic graphite (HOPG) with a WF of 4.6 eV was employed as the reference. The active area of each IHE device was measured to be approximately 0.01 mm^2, and the active area of each reference device was approximately 0.1 cm^2. The height values of the IHEs were achieved from cross-sectional FIB images and the horizontal distance values of the IHEs were measured using an optical microscope. To accurately define the photoactive area, a shadow mask with a single aperture with an area of 0.1 cm^2 was placed onto the glass side of the conventional OPVs during measurement.

B. FABRICATION OF THE IHE STRUCTURED OSCS

To prepare the IHE structures, silicon oxide substrates were cleaned ultrasonically with acetone, methanol, and deionized (DI) water in sequence for 20 min each. The residues on the silicon oxide substrates were then removed by N_2 blowing. After the cleaning process, the photoresist (AZ 5214E, Electronic Materials, USA) layers were deposited on the silicon oxide substrate by spin coating in a clean yellow light room (class 100) at a spin rate of 5,000 rpm for 40 s. The photoresist-casted substrates were dried on a hotplate at a temperature of 60 °C for 90 s in air. After the photolithography process with the photolithography mask for the ECEs, the substrates were loaded into a vacuum E-beam evaporation system and 200, 300, and 400-nm-thick layers of Al were deposited at a rate of 0.1–0.2 nm/s and a base pressure of $\sim 6 \times 10^{-7}$ h Pa. This process was repeated when the Au HCEs and 300-nm-thick Ti ECEs were fabricated. However, in the second photolithography process, the distance between the two electrodes was adjusted to 1.5 μm using alignment keys. After the photolithography process for both electrodes, solutions of the organic photovoltaic films used in this study were prepared as follows. A solution of P3HT (4002E, Rieke Metals, Lincoln, NE, U.S.A.): $PC_{60}BM$ (nano-c,TC160907 (Ph: 781-407-9417)) was prepared in Chlorobenzene (CB) (Aldrich, St. Louis, MO, U.S.A.) with a weight ratio of 1:0.7 (P3HT: $PC_{60}BM$) and a total concentration of 34 mg/ml. Before use, the P3HT: $PC_{60}BM$ solution was stirred at a temperature of 45 °C for 1 hour in a nitrogen-filled glove box. Films of P3HT: $PC_{60}BM$ were deposited by spin coating at 2000 rpm for 60 s by filtering the solution through a 0.2-μ m-pore PTFE filter. The films were then annealed at 150 °C for 30 min under a nitrogen atmosphere.

C. FABRICATION OF CONVENTIONAL STACKED OSCS

To prepare the stack structures, half-patterned ITO substrates were cleaned ultrasonically with acetone, methanol, and DI water in sequence for 20 min each. The residues on the ITO substrates were then removed by N_2 blowing. After the cleaning process, the prepared solutions were deposited on the ITO substrates by spin coating. Poly (2,3-dihydrothieno-1,4-dioxin)-poly (styrenesulfonate) (PEDOT: PSS) (4083) (Ossila, USA) was stirred at room temperature for 10 min in ambient air. After stirring for 10 min, the films of PEDOT: PSS (4083) of approximately 40-nm thick were deposited by spin coating at 5000 rpm for 60 s by filtering the solution through a 0.2-μm-pore PVDF filter. The PEDOT: PSS (4083) casted substrates were dried on a hotplate at a temperature of 110 °C for 10 min in air. The P3HT: $PC_{60}BM$ was prepared in the same way as the fabrication of the IHE OPVs. The films of P3HT: $PC_{60}BM$ of approximately 240-nm thick were deposited by spin coating at 700 rpm for 60 s by filtering the solution through a 0.2-μ m-pore PTFE filter and annealed at 150 °C for 30 min under a nitrogen atmosphere. The samples were then loaded into a vacuum thermal evaporation system (Daedong High Tech, Republic of Korea) connected to a nitrogen-filled glove box, and a 25 nm-thick layer of Ca was deposited through a shadow mask at a rate of (0.1–0.15) nm/s and a base pressure of $\sim 6 \times 10^{-8}$ h Pa. Without breaking the vacuum, a 150-nm thick Al layer was deposited through the used shadow mask at a rate of (0.1–0.2) nm/second and a base pressure of $\sim 6 \times 10^{-8}$ h Pa.

D. OSC CHARACTERIZATIONS

Current density-voltage characteristics (J–V) in the dark and under illumination were measured using a source meter (2401, Keithley Instruments, Cleveland, OH), which was controlled using the K730 program (McScience, Republic of Korea). An AM 1.5 G solar simulator (McScience, Republic of Korea) with an irradiance of $I_L = 100$ mW/cm^2 was used as the under illumination light source.

E. FINITE-DIFFERENCE TIME-DOMAIN (FDTD) SIMULATION

Optical density distributions for the different thicknesses of the P3HT: $PC_{60}BM$ layers depending on each substrate were simulated using Lumerical Solution software. The simulation domain conditions included the periodic boundary condition for the x- and y-axes, and the perfectly matched layer (PML) condition for the z-axis. The mesh size was 1 nm throughout to provide a minutely scaled design. Z and x were used as the incident light and polarization directions, respectively. Studies of absorption and scattering were estimated with the frequency-domain field and power monitor, respectively.

REFERENCES

[1] Y. Aoki, "Photovoltaic performance of organic photovoltaics for indoor energy harvester," *Organic Electron.*, vol. 48, pp. 194–197, Sep. 2017.

[2] J. H. Du *et al.*, "Efficient organic photovoltaic cells on a single layer graphene transparent conductive electrode using MoO_x as an interfacial layer," *Nanoscale*, vol. 9, pp. 251–257, Jan 7 2017.

[3] M. Kaltenbrunner *et al.*, "Ultrathin and lightweight organic solar cells with high flexibility," *Nature Commun.*, vol. 3, Apr. 2012, Art. no. 770.

[4] S.-I. Na, S.-S. Kim, J. Jo, and D.-Y. Kim, "Efficient and flexible ITO-free organic solar cells using highly conductive polymer anodes," *Adv. Mater.*, vol. 20, no. 21, pp. 4061–4067, 2008.

[5] C. Owens *et al.*, "Comparative indoor and outdoor degradation of organic photovoltaic cells via inter-laboratory collaboration," *Polymers*, vol. 8, no. 1, p. 1, 2015.

[6] C. Petridis *et al.*, "Solution processed reduced graphene oxide electrodes for organic photovoltaics," *Nanoscale Horizons*, vol. 1, no. 5, pp. 375–382, 2016.

[7] M. W. Rowell *et al.*, "Organic solar cells with carbon nanotube network electrodes," *Appl. Phys. Lett.*, vol. 88, no. 23, p. 233506, 2006.

[8] J. D. Servaites, M. A. Ratner, and T. J. Marks, "Organic solar cells: A new look at traditional models," *Energy Environ. Sci.*, vol. 4, no. 11, pp. 4410–4422, 2011.

[9] D. Kwon, M. R. Hodkiewicz, J. Fan, T. Shibutani, and M. G. Pecht, "IoT-based prognostics and systems health management for industrial applications," *IEEE Access*, vol. 4, pp. 3659–3670, 2016.

[10] S. Maity and T. Thomas, "Hole-collecting treated graphene layer and PTB7:$PC_{71}BM$-based bulk-heterojunction OPV with improved carrier collection and photovoltaic efficiency," *Proc. IEEE*, vol. 65, no. 10, pp. 4548–4554, 2018.

[11] S. Q. Zhang, Y. Zhu, J. Hou, J., "Over 14% efficiency in polymer solar cells enabled by a chlorinated polymer donor," *Adv. Mater.*, vol. 30, no. 20, p. 1800868, May 2018.

[12] D. A. Kamkar, M. Wang, F. Wudl, and T.-Q. Nguyen, "Single nanowire OPV properties of a fullerene-capped P3HT dyad investigated using conductive and photoconductive AFM," *ACS NANO*, vol. 6, no. 2, pp. 1149–1157, 2012.

[13] W. Gaynor, G. F. Burkhard, M. D. McGehee, and P. Peumans, "Smooth nanowire/polymer composite transparent electrodes," *Adv. Mater.*, vol. 23, no. 26, pp. 2905–2910, Jul. 2011.

[14] B. P. Lechêne, M. Cowell, A. Pierre, J. W. Evans, P. K. Wright, and A. C. Arias, "Organic solar cells and fully printed super-capacitors optimized for indoor light energy harvesting," *Nano Energy*, vol. 26, pp. 631–640, Aug. 2016.

[15] S. van Bavel, E. Sourty, G. de With, K. Frolic, and J. Loos, "Relation between photoactive layer thickness, 3d morphology, and device performance in P3HT/PCBM bulk-heterojunction solar cells," *Macromolecules*, vol. 42, no. 19, pp. 7396–7403, 2009.

[16] M. Lu, U. Das, and R. Birkmire, "Interdigitated back contact silicon heterojunction solar cell and the effect of front surface passivation," *Appl. Phys. Lett.*, vol. 91, no. 6, p. 063507, 2007.

[17] D. D. Smith, P. Cousins, S. Westerberg, R. De Jesus-Tabajonda, G. Aniero, and Y.-C. Shen, "Toward the practical limits of silicon solar cells," *IEEE J. Photovolt.*, vol. 4, no. 6, pp. 1465–1469, Nov. 2014.

[18] K. Yoshikawa *et al.*, "Silicon heterojunction solar cell with interdigitated back contacts for a photoconversion efficiency over 26%," *Nature Energy*, vol. 2, Mar. 2017, Art. no. 17032.

[19] S. Maity, C. T. Bhunia, and P. P. Sahu, "Improvement in optical and structural properties of ZnO thin film through hexagonal nanopillar formation to improve the efficiency of a Si–ZnO heterojunction solar cell," *J. Phys. D, Appl. Phys.*, vol. 49, no. 20, p. 205104, 2016.

[20] Q. Hou *et al.*, "Back-contact perovskite solar cells with honeycomb-like charge collecting electrodes," *Nano Energy*, vol. 50, pp. 710–716, Aug. 2018.

[21] C. T. Trinh *et al.*, "Potential of interdigitated back-contact silicon heterojunction solar cells for liquid phase crystallized silicon on glass with efficiency above 14%," *Solar Energy Mater. Solar Cells*, vol. 174, pp. 187–195, Jan. 2018.

[22] P. Büchele *et al.*, "Space charge region effects in bidirectional illuminated P3HT:PCBM bulk heterojunction photodetectors," *Organic Electron*, vol. 22, pp. 29–34, Jul. 2015.

[23] S. S. van Bavel, M. Bärenklau, G. de With, H. Hoppe, and J. Loos, "P3HT/PCBM bulk heterojunction solar cells: Impact of blend composition and 3D morphology on device performance," *Adv. Funct. Mater.*, vol. 20, no. 9, pp. 1458–1463, 2010.

[24] P. Vanlaekea *et al.*, "P3HT/PCBM bulk heterojunction solar cells: Relation between morphology and electro-optical characteristics," *Solar Energy Mater. Solar Cells*, vol. 90, no. 14, pp. 2150–2158, 2006.

[25] G. Kalita, M. Masahiro, W. Koichi, and M. Umeno, "Nanostructured morphology of P3HT:PCBM bulk heterojunction solar cells," *Solid-State Electron.*, vol. 54, no. 4, pp. 447–451, 2010.

[26] E. Kymakis *et al.*, "Carbon nanotube/PEDOT:PSS electrodes for organic photovoltaics," *Eur. Phys. J. Appl. Phys.*, vol. 36, no. 3, pp. 257–259, 2007.

[27] Yong-J. Noh, S.-I. Na, S.-S. Kim, "Inverted polymer solar cells including ZnO electron transport layer fabricated by facile spray pyrolysis," *Solar Energy Mater. Solar Cells*, vol. 117, pp. 139–144, Oct. 2013.

[28] Y. H. Kim, C. Sachse, M. L. Machala, C. May, L. Müller-Meskamp, and K. Leo, "Highly conductive PEDOT:PSS electrode with optimized solvent and thermal post-treatment for ITO-free organic solar cells," *Adv. Funct. Mater.*, vol. 21, pp. 1076–1081, 2011.

[29] W. Tress, K. Leo, and M. Riede, "Influence of hole-transport layers and donor materials on open-circuit voltage and shape of *I–V* curves of organic solar cells," *Adv. Funct. Mater.*, vol. 21, no. 11, pp. 2140–2149, 2011.

[30] J. Y. Kim *et al.*, "New architecture for high-efficiency polymer photovoltaic cells using solution-based titanium oxide as an optical spacer," *Adv. Mater.*, vol. 18, no. 5, pp. 572–576, 2006.

[31] N. Wu, Q. Luo, Z. Bao, J. Lin, Y.-Q. Li, C.-Q. Ma, "Zinc oxide: Conjugated polymer nanocomposite as cathode buffer layer for solution processed inverted organic solar cells," *Solar Energy Mater. Solar Cells*, vol. 141, pp. 248–259, Oct. 2015.

[32] Y. Zhou *et al.*, "A universal method to produce low–work function electrodes for organic electronics," *Science*, vol. 336, no. 6079, pp. 327–336, 2012.

YOUNG-JUN YOU was born in Seoul, South Korea, in 1991. He received the B.S. degree in electronics and electrical engineering from Dongguk University, Seoul, in 2017, where he is currently pursuing the M.S. degree in microelectronics engineering. From 2016 to 2017, he was an undergraduate research student with the Organic Nano Device Laboratory, Seoul. His research interests include organic devices, photovoltaic devices, especially organic solar cells, which have high efficiency under indoor light sources, and their applications.

DO YOUNG KIM was born in Busan, South Korea, in 1992. He is currently pursuing the B.S. degree in electronic and electrical engineering at Dongguk University, Seoul, South Korea. From 2013 to 2014, he served as KATUSA (Korean Augmentation to the United States Army) and retired as a sergeant from the military service. From 2017 to 2018, he was an undergraduate research student with the Organic Nano Device Laboratory, Seoul. His research interests include fabrication of new organic and inorganic and hybrid materials-based devices, photovoltaic devices, light emitting devices, thin film transistors, and printable flexible devices.

SANG-CHUL SHIN was born in Daejeon, South Korea, in 1991. He received the B.S. degree in electronics and electrical engineering from Dongguk University, Seoul, South Korea, in 2017, where he is currently pursuing the M.S. degree in microelectronics engineering. He was at the Korea Institute of Machinery & Materials, Daejeon, as an experiment assistant, for two months, from July to August, in the year 2015. From 2016 to 2017, he was an undergraduate research student with the Organic Nano Device Laboratory, Seoul. His research interests include organic devices, photovoltaic devices, especially organic photovoltaics which have high efficiency, large scale, and characteristic analysis under indoor light sources, and their applications.

JAE WON SHIM was born in Seoul, South Korea, in 1980. He received the B.S. degree in electrical engineering from Korea University, Seoul, in 2005, the M.S. degree in electrical and computer engineering from The University of Texas at Austin, Austin, TX, USA, in 2008, and the Ph.D. degree in electrical and computer engineering from the Georgia Institute of Technology, Atlanta, GA, USA, in 2014. From 2014 to 2015, he was a Research Staff Member with the Samsung Advanced Institute of Technology. Since 2015, he has been an Assistant Professor with the Division of Electronics and Electrical Engineering, Dongguk University, Seoul. He has more than 10 years of research experience in the field of organic electronic devices. His current research interests include investigation of fundamental physical processes (charge transport, light harvesting, and emission) in organic-based nanostructured thin films, to the design, fabrication, and testing of light-weight flexible optoelectronic devices based on hybrid printable materials.